ORIGINAL PAPER

Determining maize water stress through a remote sensing-based surface energy balance approach

Edson Costa-Filho[1] · José L. Chávez[1] · Louise Comas[2]

Abstract

Determining water stress levels of vegetated surfaces is crucial for irrigation scheduling. This paper aims to evaluate a new method for obtaining crop water stress index (CWSI) based on the estimation of sensible heat flux using an aerodynamic temperature gradient approach. Data were collected on a deficit irrigated maize field at a research farm located in Greeley, Colorado, USA, in 2017 and 2018. The irrigation treatment used subsurface drip. Weather data were measured on-site at 3.3 m above ground level. RED and NIR surface reflectance data were obtained on-site through multispectral radiometer measurements. Nadir surface temperature data were measured using infra-red thermometers at 1 m above canopy. CWSI estimated values were used to assess daily soil water stress index (SWSI), calculated from measurements of volumetric soil water content (VWC) and management allowed depletion (MAD) of 40%. Results show that SWSI is best represented through a non-linear rational CWSI function. Modeled CWSI estimates were compared to measured surface heat fluxes, resulting in a mean bias error of -0.02 and a root mean square error of 0.09, while errors were 0.02 and 0.06 when compared with observed CWSI based on canopy transpiration measured with plant sap flow devices. Results seem to validate the proposed sensible heat flux-based CWSI model. The CWSI approach presented could be used to manage irrigation and conserve water resources for maize in semi-arid regions.

Introduction

Irrigation scheduling and agricultural water management practices have shifted toward optimizing crop yield and conserving water and soil resources due to climate change and population growth. Maize is an essential commodity across the United States of America (USA). The susceptibility of yield loss due to the climate change conditions is evident across the USA. These conditions affect most productive crops, including maize. According to Chung et al. (2014), maize yield in the USA could suffer a reduction of 29% due to changes in climate that are caused by accentuating extreme conditions (i.e., droughts) by 2050. Within the countryside, the areas that are more susceptible to suffer intense drought seasons due to future reduced rainfall and snowmelt events are the locations within the Midwest of the USA, which include, but not limited to, Kansas, Iowa, Nebraska, and Oklahoma (Tubiello et al. 2002). Most of the maize production in the country is concentrated in this geographic region, according to USDA National Agricultural Statistical Service (USDA—NASS) 2017 report. The need to increase agricultural water management practices for maize to preserve water and minimize the effects of drought seasons relies on the development of more efficient methods to assess stress levels that might integrate surface heterogeneity due to soil properties' differences and canopy resilience to water stress conditions.

Crop water stress level assessment has been used as a decision-making tool for triggering irrigation water applications during the vegetative growth stage of crops. Early studies suggested that the temperature gradient between the canopy and air temperatures was correlated to the degree

✉ José L. Chávez
jose.chavez@colostate.edu

Edson Costa-Filho
edscos@rams.colostate.edu

Louise Comas
Louise.Comas@usda.gov

[1] Civil and Environmental Engineering Department, Colorado State University, Fort Collins, CO 80523, USA

[2] United States Department of Agriculture, Agricultural Research Service (USDA-ARS), Fort Collins, CO 80526, USA

of stress that the plants suffer when the soil water content within the root zone is continually depleted over time (Idso et al. 1977; Ehrler et al. 1978; Jackson et al. 1981).

Induced canopy water stress due to weather conditions or irrigation management practices might be assessed through the calculation and analysis of water-stressed indices. In the literature, several indices could be related to canopy water stress levels such as aeration (ASI), drought (DSI), harvest (HSI), crop water (CWSI), and soil water (SWSI) stress indices (Wang et al. 2015; Jackson et al. 1988; Chávez 2015). Calculations of aeration and drought stress indices depend on soil matrix properties and water content characteristics. The harvest stress index is a function of the rates of evapotranspiration from water and non-water stress conditions, as well as a given minimum harvest index that should vary among different crop types (Wang et al. 2015). The SWSI is an index that also relies on soil water properties. Still, it adds a component associated with irrigation water management practices for a given vegetation type into the estimation of the water stress index. The additional term is based on a soil water content threshold for triggering irrigation (Chávez 2015), which makes the water stress level's prediction closer to the field conditions than previous soil water-based stress indices listed. The crop water stress index relies on the estimation of canopy stress levels that are based on the interaction of a given surface and surrounding atmosphere conditions, such as the canopy and air temperatures and surface heat fluxes.

The ASI, DSI, HSI, and SWSI determination depends on point source (small area/volume) measurements throughout the root zone. For a point-basis analysis, the accuracy of the stress index methods based on soil water measurements is an advantage to be considered. However, the assessment of spatial water stress for large plots with heterogeneous soil–plant properties is not reliable due to the need for data collection at several different locations across an agricultural field. Logistics and financial issues could be a byproduct of the need for more data and limit soil water-based stress indices' application for agricultural water management.

The CWSI method has been widely implemented to monitor and improve irrigation water management spatially because of the easiness of acquiring the data needed across an entire field. Some studies in the literature indicate different researches that describe methods to calculate CWSI based on remotely sensed data acquisition for temperature and biomass (O'Shaughnessy et al. 2011; Wang et al. 2016; Sagayo et al. 2017; Jiang et al. 2018). The CWSI method is reliable to characterize better canopy water stress conditions in different agricultural fields that demand different decision-making processes based on the canopy water demand at different locations within the area. Limiting factors such as availability, both on quantitative and qualitative terms, of images and technical expertise to use algorithms might

impose challenges on the dissemination of CWSI remotely sensed algorithms. However, advancements in research and imagery resolution through unmanned aircraft tend to overcome the limitations of implementing CWSI algorithms.

The amount of water that is depleted from the surface through plant transpiration and soil water evaporation is a function of environmental variables such as net radiation (R_n), vapor pressure deficit (VPD), wind speed (u), and water availability in the soil profile (Idso et al. 1981). Existing methods for determining crop water stress index relied on measurements of canopy temperature using infrared thermometers (IRT). IRT is an instrument capable of providing on-site temperature data based on the thermal emission of radiation by the surface. The early CWSI calculation was based on Eq. (1), Jackson et al. (1988):

$$\text{CWSI}_o = \frac{(T_c - T_a) - (T_{\text{wet}} - T_a)}{(T_{\text{dry}} - T_a) - (T_{\text{wet}} - T_a)}, \tag{1}$$

where CWSI_o represents the crop water stress index initial developed approach (dimensionless); T_c refers to the canopy or leaf temperature (°C or K); T_{wet} is the canopy temperature (°C or K) for when the plant is experiencing no water limitations and operating at a full transpiration rate; T_{dry} is the canopy temperature when the plant is no longer transpiring (°C or K), and T_a is the air temperature at a screening height above the canopy (°C or K).

Ben-Gal et al. (2009) have indicated that CWSI might be calculated empirically or analytically. Empirical methods' accuracy is highly dependent on the precision of temperature measurements and the adequate estimation of T_{dry} and T_{wet} that are often associated with the field conditions. These canopy temperatures, however, do not have standardized thresholds for defining when the surface is considered dry or wet enough to be representative for the water stress level assessment. Analytical methods attempt to overcome the issues with uncertainties derived by the dry and wet conditions based on the incorporation of R_n, sensible heat (H), and latent heat (LE) fluxes from the surface energy balance, as indicated by Jones (1999). When compared to temperature-based methods, surface heat flux approaches to estimate CWSI tend to represent better the influence of climate conditions, soil type, and canopy characteristics on addressing the levels of water stress for plants. It is because addressing the different incoming and outgoing sources of heat might introduce several different variables that describe dynamic processes that induce canopy water stress.

Based on those concepts, there have been approaches to calculate CWSI that incorporate more environmental variables into the assessment of water stress conditions for vegetated surfaces. Osroosh et al. (2015) have presented a method to determine analytical CWSI based on the work of Idso et al. (1981) that introduces R_n, wind speed, and

VPD into the modeling process for CWSI, combined with a time-threshold method to assess when irrigation water should be scheduled.

O'Shaughnessy et al. (2011) have shown the applicability of remote sensing thermography and thermometry into providing reliable estimates of canopy stress levels based on the radiometric surface temperature obtained from the image processing for soybeans and cotton. Zarco-Tejada et al. (2013) have applied remote sensing methods to assess empirical CWSI using thermal band images coupled with photochemical reflectance index (PRI) that accounts for the biomass architectural and healthiness conditions of the canopy.

Sensible heat and latent heat fluxes are interconnected as on-site environmental and soil water availability conditions are dynamically changing over space and time. The ratio between sensible and latent heat fluxes, proposed by Bowen (1926), was named the Bowen ratio (β_o). This ratio gives physical meaning to the effects of water stress on the magnitude of those surface heat fluxes. Taiz et al. (2015) mentioned that when the soil profile has limited (stored) water content, the magnitude of β_o is more substantial than when no stress conditions are predominant. Therefore, well-watered field conditions allow the magnitude of LE to be higher than H, while aggravated water deficit over time leads latent heat fluxes to be smaller than sensible heat fluxes.

When water content within the root zone is available to meet canopy hydration demands, micrometeorology conditions of the field have a powerful impact on the dynamics of vapor and heat transfer. However, when stress conditions do not allow the crop to physically extract the amount of water needed to keep photosynthesis and other internal biochemical processes under their natural ongoing stages, soil properties will significantly influence the physical processes that derive H and LE. Thus, there is an increase in leaf water suction potential that causes transpiration to be reduced over time (Gardner and Ehlig 1963).

As an alternative approach to estimate CWSI, this paper introduces a surface energy balance approach based on weather and remote sensing data. The primary consideration for such method is to explore the intrinsic association between canopy water stress and its impact on the magnitude of sensible heat flux and the remaining components of the surface energy balance. The proposed approach is based on aerodynamic surface temperature (T_o) modeling to estimate sensible heat flux, a critical element for the single-source H model. Thus, the objectives of this paper are as follows: (a) to apply a surface aerodynamic temperature-based energy balance method to estimate maize water stress (CWSI); (b) to assess the proposed CWSI model's applicability for mapping water stress levels across an agricultural field; and (c) to evaluate SWSI curve-fitting models, for extrapolating stress levels from a point-source to a spatial scale based on the estimation of CWSI.

Materials and methods

Experiment site description

The experimental site was the Limited Irrigation Research Farm (LIRF) managed by the United States Department of Agriculture—Agricultural Research Service (USDA-ARS) in Greeley, Colorado, USA; latitude N 40.4463°, longitude W 104.6371°, and elevation of 1432 m (Fig. 1). Data were collected in 2017 and 2018 from the end of July to September.

The canopy underwent water stress due to low-frequency irrigation water application. Only two major irrigation events were scheduled for the water-stressed treatment. Field 1 and field 2 were the low-frequency irrigation plots in 2017 and 2018, respectively (Fig. 1). Irrigation events were timed by crop characteristics such that the first irrigation was 2–3 weeks before anthesis/pollination to assure getting to full-ground cover, and the second irrigation was in the late milk kernel stage. The field dimensions were 190 m×110 m. The maize variety was Dekalb 51–20 (drought tolerant) for both years with irrigation supplied by subsurface drip. The drip irrigation emitters were 0.30 m apart and buried 0.23 m deep on 0.76 m distance between rows. Plant density was 87,500 plants per hectare. Tillage was accomplished by strip-tilling before planting, which occurred on DOY 152 and 130 in 2017 and 2018, respectively. Nitrogen fertilizer was applied as urea ammonium nitrate (UAN) at 32% concentration rate. In 2017, nitrogen was applied on DOY 186 and 213, at a rate of 39 and 76 kilograms per hectare, respectively. For the 2018 season, nitrogen was used on DOY 197 and 226 at a rate of 72 and 50 kilograms per hectare, respectively. Irrigation scheduling followed the paper FAO-56 standard approach method (Allen et al. 1998), based on crop coefficient and reference alfalfa ET calculated as indicated by ASCE-EWRI (2005). The basal maize crop coefficient (k_{cb}) was regional coefficient based on the work developed by Garcia et al. (2013). The stress coefficient (k_s) determination was based on the relationship among total available water (TAW), readily available water (RAW), and soil water deficit (D_r).

Data collection and instrumentation

The measurements of required data to derive SWSI and to model and assess CWSI estimation were done using a total of 42 sensors. Table 1 shows the type of sensors used, in 2017 and 2018, for the measurements needed for the estimation and assessment of modeled CWSI at LIRF.

Fig. 1 Top view of the fields at LIRF nearby Greeley, CO

Table 1 Summary of sensors used at LIRF in 2017 and 2018

Sensor type	Model type	Manufacturer name	Manufacturer location
Soil water content	Mini-Trace 6085	Soil moisture Equipment	Santa Barbara, CA, USA
Multispectral radiometer	MSR5	Cropscan, Inc.	Rochester, MN, USA
Soil water content	5TE	Decagon Devices, Inc.	Pullman, WA, USA
Infra-red thermometer	SI-111	Apogee Instruments	Logan, UT, USA
T_a and relative humidity (RH)	HMP45C	Vaisala	Vantaa, Finland
Wind speed cup anemometer	03101-L	RM Young Company	Traverse City, MI, USA
Net radiometer	NR-Lite	Kipp and Zonen	Delft, The Netherlands
Net radiometer	CNR01	Kipp and Zonen	Delft, The Netherlands
Soil heat flux plate	HFT3-L	Radiation and Energy Balance Inc.	Bellvue, WA, USA
Canopy analyzer	LAI 2000	LICOR	Lincoln, NE, USA
Sap flow meter	EXO Sensors	Dynamax, Inc.	Houston, TX, USA

On-site weather data

Weather data for managing irrigation were obtained from the Colorado Mesonet Agricultural Weather Station Network (CoAgMet) station Greeley 04 (GLY04), which is located within the research facility. The GLY04 station is located on a well-watered 12-cm height clipped grass field. On-site weather data for modeling R_n and H were collected every minute and averaged every 15 min from aerodynamic tower stations (SAT) located, 8 m from the northwest (NW) corner of the field. The location of the SAT stations was chosen to allow better fetch conditions for the mixing of air and its interaction with the surface, considering that wind speed direction at the research facility site is mainly from southwest. These data included wind speed, T_a, and relative humidity (RH), measured using cup anemometers and hygrometers, respectively, at the height of 3.3 m above ground level (AGL).

On-site remote sensing data

Remote sensing data were acquired on-site through point measurements using handheld and on-site stationary sensors/stations. Periodic readings were taken over the maize surface at nadir. These readings included radiometric surface temperature (T_s), near-infrared (NIR), and red (RED) surface reflectance. Surface temperature was measured every minute and data were averaged every 15 min at two measurement stations with SI-111 IRTs (Apogee Instruments, Logan, UT, USA) located, respectively, at about 1/4 and 1/2 total length of the field from the north side (Fig. 2). The measurements were averaged between the two stations to provide a symbolic value of surface temperature for the entire field area. Surface reflectance data were measured once a week in 2017 and twice a week in 2018 at 1/4, 1/2, and 3/4 total length of the field and averaged to represent the entire area of study.

On-site soil water content data

Volumetric soil water content (VWC) measurements were collected using 5TE water content, temperature, and electrical conductivity sensor (Decagon Devices, Pullman, WA, USA). Soil water content data were used to calculate the soil water stress index (SWSI) for the CWSI model comparison. Measurements of VWC were done at each on-site measurement station at depths of 4, 20, 50, 80, and 110 cm (Fig. 3).

VWC data from 5TE sensors at 4 cm depth were cross-calibrated, per location, using mini-trace time-domain
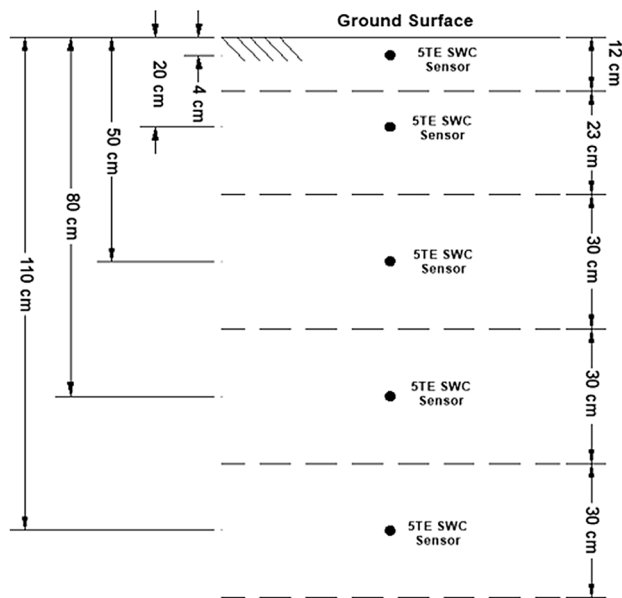

Fig. 3 Root zone profile and the soil water content sensors installed at respective depths and soil layer thickness

reflectometer (TDR) data. The VWC data for other depths were adjusted based on neutron probe (NP) VWC measurements, which were taken once and twice a week in 2017 and 2018, respectively. The TDR and NP readings were done at the following depths: 0.15, 0.30, 0.60, 0.90, and 1.20 m. The resulting linear calibration approach was applied to adjust

Fig. 2 Schematic of the layout of the on-site measurement stations at LIRF in 2017 and 2018
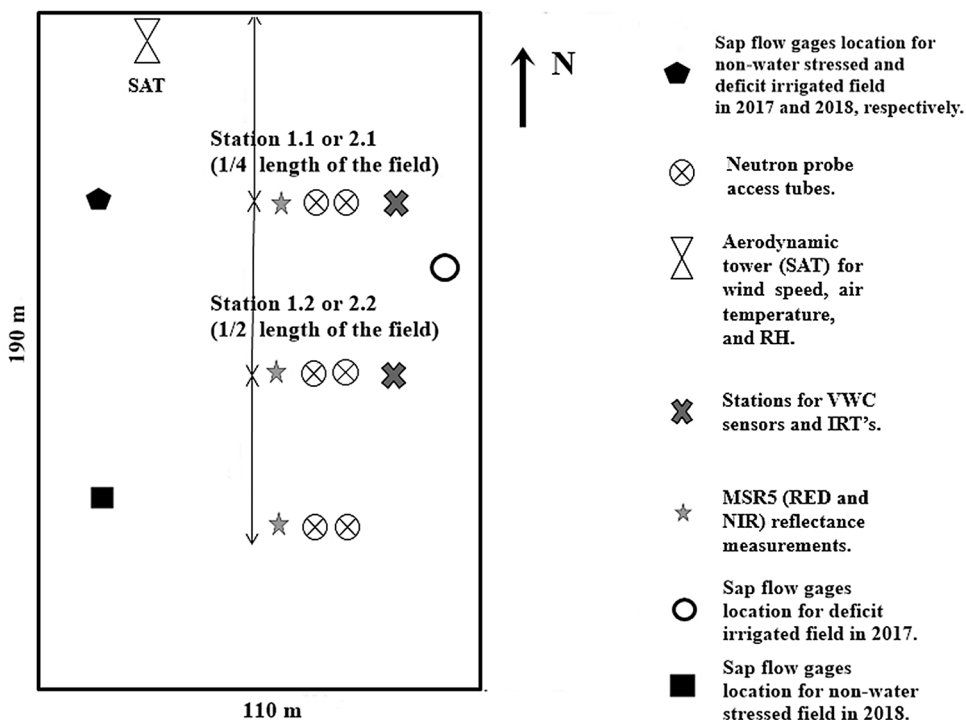
the measured data from the 5TE sensors, as indicated by Eq. (2):

$$\text{VWC}_i = a_1 \text{VWC}_{5\text{TE}} + a_2, \tag{2}$$

where $\text{VWC}_{5\text{TE}}$ represents the volumetric water content from 5TE sensor (m^3/m^3), VWC_i refers to the volumetric water content from TDR or NP (m^3/m^3), and a_1 and a_2 are the empirical fitted coefficients for the linear calibration model. The TDR and NP readings were done once and twice a week, respectively, in 2017 and 2018.

Calculation of CWSI

The calculation of CWSI might be approached as indicated by Eq. (3):

$$\text{CWSI} = 1 - \frac{\text{ET}_a}{\text{ET}_c} = \frac{\text{ET}_c - \text{ET}_a}{\text{ET}_c}, \tag{3}$$

where ET_a and ET_c refer to actual evapotranspiration (mm) and crop evapotranspiration (mm), respectively, for well-watered field conditions.

When rewriting Eq. (3) in terms of energy density flux, CWSI could be determined as

$$\text{CWSI} = \frac{\lambda_w \text{ET}_c - \lambda_w \text{ET}_a}{\lambda_w \text{ET}_c} = \frac{\text{LE}_c - \text{LE}_a}{\text{LE}_c}, \tag{4}$$

where λ_w is the latent heat of vaporization of water (J/Kg), LE_a and LE_c are, respectively, the actual latent heat flux (W/m^2) and the latent heat flux for unstressed water conditions (W/m^2).

When the crop does not undergo water stress conditions, $\text{ET}_a \sim \text{ET}_c$ and that results on CWSI = 0. As the soil water content of the root zone starts to be depleted over time with no root zone recharge from rain or irrigation events, the root depth storage capacity of the soil profile results in $\text{ET}_a < \text{ET}_c$ and $0 < \text{CWSI} < 1$.

Actual evapotranspiration might be written in terms of latent heat flux, as the residual of the surface energy balance approach, indicated by Eq. (5):

$$\text{LE}_a = R_n - G - H. \tag{5}$$

Evapotranspiration for non-stressed conditions occurs when all available energy ($R_n - G$) is used for evaporating water from the topsoil and transpiring water from the canopy. Thus, when there are no limitations in water availability within the root zone, the plants will transpire at higher rates and the soil will gradually lose water mass due to evaporation, which results in having smaller values of sensible heat flux in comparison to available energy. Therefore, it is reasonable to indicate the latent heat flux for fully unstressed

water conditions as equivalent to the available energy, as indicated by Eq. (6):

$$\text{LE}_c \approx R_n - G. \tag{6}$$

Substituting Eqs. (5) and (6) in Eq. (4), CWSI is then calculated as a function of sensible heat flux and available energy, as follows:

$$\text{CWSI} = \frac{(R_n - G) - (R_n - G - H)}{(R_n - G)} = \frac{H}{R_n - G}. \tag{7}$$

Spectral remote sensing indices' calculation

The following spectral remote sensing indices were incorporated, alongside with radiometric surface temperature, to estimate sensible heat flux and available energy: normalized difference vegetation index (NDVI), optimized soil adjusted vegetation index (OSAVI), leaf area index (LAI), and fractional percent cover (f_c).

NDVI is calculated as indicated by Eq. (8):

$$\text{NDVI} = \frac{\text{NIR} - \text{RED}}{\text{NIR} + \text{RED}}. \tag{8}$$

OSAVI was developed by Rondeaux et al. (1996) as an attempt to minimize the effects of soil background on surface reflectance readings, and it is indicated by Eq. (9):

$$\text{OSAVI} = \frac{(\text{NIR} - \text{RED})(1 + L)}{(\text{NIR} + \text{RED} + L)}, \tag{9}$$

where L is the adjusted factor term that reduces the noise caused by the soil reflectance on the vegetation index, and it depends on LAI ranges. An average value of L for most soil was assumed to be 0.16 (Rondeaux et al. 1996).

Leaf area index (LAI) was calculated based on the work developed by Chávez et al. (2010), Eq. (10):

$$\text{LAI} = 0.263 e^{(3.813 \text{OSAVI})}. \tag{10}$$

Fractional percent cover was estimated following the empirical linear model developed by Johnson and Trout (2012), which relates NDVI to vegetation cover percent:

$$f_c = \begin{cases} 0, \text{NDVI} < 0.15 \\ 1.26\text{NDVI} - 0.18, \text{NDVI} \geq 0.15 \end{cases}. \tag{11}$$

NDVI and OSAVI were initially calculated using measured (around noon time) RED and NIR surface reflectances, at different locations in the field, and were averaged and assumed representative for a given day. It was assumed that multispectral surface reflectance changes due to solar angle and environmental effects such as cloudiness conditions, wind speed, and temperature might have small

effects on reflectance values around noontime (11 am to 3 pm MST). Thus, small changes in NDVI and OSAVI values were neglected and the indices were assumed to be constant from 11 am to 3 pm. The MSR5 multispectral radiometer detects incoming shortwave radiation (up looking sensors) and reflected radiation (down looking sensors). MSR5-derived surface reflectance measurements (after processing) include sun angle corrections, which minimize the differences in surface reflectance around solar noontime.

For days without measurement, NDVI and OSAVI were estimated through non-linear empirical equations fitted using MATLAB curve fitting toolbox feature, considering on-site data measurements, for each year, by having the day of the year (DOY) as a predictor, Eqs. (12) to (15):

$$\text{NDVI}_{17} = 0.802 \sin(0.024\text{DOY} + 2.107), \tag{12}$$

$$\text{NDVI}_{18} = 0.783 \sin(0.028\text{DOY} + 1.433), \tag{13}$$

$$\text{OSAVI}_{17} = 0.674 \sin(0.024\text{DOY} + 2.036), \tag{14}$$

$$\text{OSAVI}_{18} = 0.680 \sin(0.029\text{DOY} + 7.516), \tag{15}$$

where NDVI_i and OSAVI_i refer to vegetation index for a particular year. Subscripts 17 and 18 refer to the years of 2017 and 2018, respectively.

Net radiation modeling

Net radiation was calculated following the radiation budget (long and short waves) approach:

$$R_n = (1 - \alpha)R_s - \varepsilon_s \sigma T_{sK}^4 + \varepsilon_s \varepsilon_a \sigma T_{aK}^4, \tag{16}$$

where α refers to surface albedo, R_s is solar radiation or incoming shortwave radiation (W/m²), ε_a and ε_s are air and surface thermal emissivities, respectively; T_{aK} and T_{sK} are air and surface temperature (K), respectively; and σ refers to the Stefan–Boltzmann constant (5.67×10^{-8} W/m²/K⁴).

Solar radiation data were obtained on-site, for both years, using the 4-way net radiometer installed at 3.2 m AGS. Albedo was estimated following a non-linear empirical equation ($r^2 = 0.75$) developed through MATLAB curve fitting toolbox feature and based on on-site data, in 2018, that relates α measured by the 4-way net radiometer and LAI measured data collected using the LICOR LAI 2000 m:

$$\alpha = 0.016\text{LAI}^{(-2.135)} + 0.179. \tag{17}$$

Air emissivity was calculated based on the work of Crawford and Duchon (1999), a modification of Brutsaert (1975) to account for cloudiness conditions of the field:

$$\varepsilon_a = \left[\text{clf} + (1 - \text{clf})(1.22 + 0.06 \sin\left([\text{mo} + 2]\frac{\pi}{6}\right)\right]\left(\frac{e_a}{T_{aK}}\right)^{1/7}, \tag{18}$$

where clf is the cloud fraction term, mo refers to the month of the year (e.g., January = 1 February = 2), and e_a is the actual vapor pressure in mb.

Surface emissivity (ε_s) was estimated using Eq. (19) after Brunsell and Gillies (2002); in which, for a given surface (vegetation and exposed soil), it is represented as a function of the fractional vegetation cover:

$$\varepsilon_s = 0.98f_c + 0.93(1 - f_c), \tag{19}$$

where 0.98 is chosen as the surface emissivity of a fully vegetated area and 0.93 is assumed to be the surface emissivity of bare soil.

Soil heat flux modeling

Soil heat flux was estimated following the semi-empirical model developed by Bastiaanssen et al. (1998) that relates G to surface remote sensing vegetated indices and net radiation:

$$G = \frac{T_s}{\alpha}\left(0.0032\alpha + 0.0062\alpha^2\right)\left(1 - 0.978\text{NDVI}^4\right). \tag{20}$$

Sensible heat flux modeling

The modeling for sensible heat flux is performed based on the bulk aerodynamic resistance approach, Eq. (21):

$$H = \rho_a Cp_a\left(\frac{T_o - T_a}{r_{ah}}\right), \tag{21}$$

where ρ_a stands for air density (kg/m³), Cp_a is the specific heat of the air (~ 1005 kg/J/K), r_{ah} is the aerodynamic resistance (s/m), and T_o and T_a are aerodynamic surface temperature (°C) and air temperature (°C), respectively.

Calculation of aerodynamic resistance

When the atmosphere is under adiabatic conditions, r_{ah} is calculated by Eq. (22):

$$r_{ah} = \frac{\ln\left(\frac{Z_m - d}{Z_{om}}\right)\ln\left(\frac{Z_m - d}{Z_{oh}}\right)}{u_m k^2}, \tag{22}$$

where Z_m is the wind speed height of measurement (m), u_m is the measured wind speed at Z_m AGL (m/s), and k is the Von Karman constant (0.41).

For atmospheric conditions when the surface is warmer (unstable) or cooler (stable) than the surrounding air, r_{ah}

calculation must include a stability correction factor to adjust to real conditions. Equation (23) indicates the adjusted r_{ah} model (Yasuda 1988):

$$r_{ah} = \frac{\ln\left(\frac{Z_m - d}{Z_{oh}}\right) - \psi_h}{u_* k}, \tag{23}$$

where u_* is the friction velocity (m/s), ψ_h the atmospheric stability correction function for heat transfer, and Z_{oh} the roughness length for heat transfer (m).

The stability atmospheric correction function for heat transfer is given by Eq. (24) for unstable conditions (Yasuda 1988):

$$\psi_h = 2\ln\left(\frac{1 + x_2^2}{2}\right) - 2\ln\left(\frac{1 + x_1^2}{2}\right), \tag{24}$$

$$x_1 = \left[1 - \frac{16(Z_m - d)}{L_{MO}}\right]^{0.25}, \tag{25}$$

$$x_2 = \left[1 - \frac{16 Z_{oh}}{L_{MO}}\right]^{0.25}, \tag{26}$$

where L_{MO} refers to the Monin–Obukhov stability length factor (m).

The Monin–Obukhov stability length variable was named after the work of Monin and Obukhov (1954), based on similarity theory, and it is calculated as

$$L_{MO} = -\frac{u_*^3 T_a \rho_a C p_a}{g k H}, \tag{27}$$

where g is the gravity acceleration (9.81 m/s²).

According to Yasuda (1988), ψ_h is given by Eq. (28) for stable atmospheric conditions:

$$\psi_h = 6\ln\left(1 - \frac{Z_m}{L_{MO}}\right)\left[\frac{Z_{om}}{L_{MO}} - \frac{Z_m - d}{L_{MO}}\right]. \tag{28}$$

Calculation of friction velocity

Friction velocity might be estimated, under neutral atmospheric conditions using Eq. (29)

$$u_* = \frac{u_m k}{\ln\left(\frac{Z_m - d}{Z_{om}}\right)}, \tag{29}$$

where Z_{om} is the roughness length for momentum transfer (m); explained in the next section.

For non-neutral atmospheric conditions (Yasuda 1988)

$$u_* = \frac{u_m k}{\ln\left(\frac{Z_m - d}{Z_{om}}\right) + \psi_m}, \tag{30}$$

where ψ_m is the atmospheric stability correction function for momentum transfer (m).

When the atmospheric conditions are considered unstable, ψ_m is calculated as indicated by Eq. (31):

$$\psi_m = \psi_{m2} - \psi_{m1}, \tag{31}$$

where

$$\psi_{m1} = 2\ln\left(\frac{1 + x_1}{2}\right) + \ln\left(\frac{1 + x_1^2}{2}\right) - 2\arctan(x_1) + \frac{\pi}{2}, \tag{32}$$

$$\psi_{m2} = 2\ln\left(\frac{1 + x_3}{2}\right) + \ln\left(\frac{1 + x_3^2}{2}\right) - 2\arctan(x_3) + \frac{\pi}{2}, \tag{33}$$

$$x_3 = \left[1 - \frac{16 Z_{om}}{L_{MO}}\right]^{0.25}. \tag{34}$$

For stable atmospheric conditions, it is assumed that $\psi_h = \psi_m$.

Calculation of roughness canopy elements

Zero-displacement height and roughness lengths for momentum and heat transfer might be calculated using remote sensing approaches that incorporate variables about surface biomass conditions into modeling. Zero-displacement height and roughness length for momentum transfer were calculated as indicated by Choudhury and Monteith (1988) based on a model that incorporates LAI and canopy height as predictors. Equations (35) and (36) state, respectively, the models for d and Z_{om}.

$$d = h_c\left[\ln\left(1 + X^{\frac{1}{6}}\right) + 0.03\ln\left(1 + X^6\right)\right], \tag{35}$$

$$Z_{om} = \begin{cases} Z_o' + 0.28 h_c\sqrt{X}, & 0 \le X \le 0.20 \\ 0.3 h_c\left(1 - \frac{d}{h_c}\right), & 0.20 < X \le 2 \end{cases}, \tag{36}$$

where $X = 0.20$ LAI; Z_o' is the roughness length of the soil surface and assumed to be 0.01 m; and h_c is the canopy height (m).

Roughness length for heat transfer is often taken as 10% of Z_{om} (Brutsaert 1982). Canopy height was calculated based on an empirical non-linear exponential model developed using on-site measured data that relate h_c to LAI, as indicated by Eq. (37) ($r^2 = 0.91$):

$$h_c = 0.697e^{(0.236\text{LAI})} - 3.42e^{(-3.177\text{LAI})}. \tag{37}$$

Aerodynamic surface temperature modeling

The surface aerodynamic temperature (T_o) was estimated based on the approaches developed by Costa-Filho (2019). Models of T_o were developed based on multiple linear equations that incorporate remote sensing variables and weather data as predictors. Equation (38) is the aerodynamic temperature model used in the sensible heat flux equation,

$$T_o = \begin{cases} -8.742f_c + 0.571T_a + 0.529T_s + 0.806r_p + 3.295, & 0.85 \le \text{LAI} \le 1.50 \\ -9.168f_c + 0.485T_a + 0.575T_s - 0.160r_p + 6.491, & 1.50 < \text{LAI} \le 2.50 \\ 4.708f_c + 0.350T_a + 0.580T_s + 0.086r_p, & 2.50 < \text{LAI} \le 3.50 \\ -1.912f_c + 0.443T_a + 0.509T_s + 0.115r_p + 5.014, & 3.50 < \text{LAI} \le 5.00 \end{cases}. \tag{38}$$

where r_p refers to turbulence mixing-row resistance (s/m).

The r_p variable was developed by Costa-Filho (2019) as an attempt to incorporate the interactions between crop row layout and air flowing above the canopy into the modeling of sensible heat flux. It might be calculated, for row crops oriented north–south, as following:

$$r_p = \begin{cases} \left(\frac{\theta_u}{180^o - \theta_u}\right)\left(\frac{1}{u_m}\right), & 0° \le \theta_u \le 90° \\ \left(\frac{180^o - \theta_u}{\theta_u}\right)\left(\frac{1}{u_m}\right), & 90° < \theta_u \le 180° \\ \left(\frac{\theta_u - 180^o}{360^o - \theta_u}\right)\left(\frac{1}{u_m}\right), & 180° < \theta_u \le 270° \\ \left(\frac{360^o - \theta_u}{180^o - \theta_u}\right)\left(\frac{1}{u_m}\right), & 270° < \theta_u \le 360° \end{cases} \tag{39}$$

where θ_u is the wind speed direction in degrees.

Data for sensible heat flux modeling were filtered for wind speed direction to avoid the influence of nearby areas that are not the same surface type as the corn fields used for the experiment. Only wind speed direction ranges from 110° to 160° and 200° to 250° were considered since those directions allow the air to flow through longer distances above the maize fields.

Calculation of SWSI

Daily soil water stress index was estimated from measured soil water content data on-site as determined by Chávez (2015):

$$\text{SWSI} = \begin{cases} \frac{\text{VWC}_t - \text{VWC}_a}{\text{VWC}_t - \text{VWC}_{\text{WP}}}, & \text{VWC}_t > \text{VWC}_a \\ 0, & \text{VWC}_t \le \text{VWC}_a \end{cases}, \tag{40}$$

where VWC_t, VWC_a, and VWC_{WP} refer to, respectively, volumetric water content threshold for triggering irrigation (m^3/m^3), the actual measured volumetric water content in the root zone (m^3/m^3), and volumetric water content at permanent wilting point (m^3/m^3).

The volumetric water content threshold for irrigation purposes is calculated as indicated by Eq. (41):

$$\text{VWC}_t = \text{MAD} \left(\text{VWC}_{\text{FC}} - \text{VWC}_{\text{WP}}\right) \tag{41}$$

where MAD means management allowed depletion and VWC_{FC} is the volumetric water content at field capacity (m^3/m^3).

Field capacity data were obtained using on-site volumetric water content from neutron probe readings a few days after a significant rainfall or irrigation event. For the year 2017, volumetric water content measured on DOY 226 was considered VWC_{FC} due to a 29 mm rainfall event that occurred on DOY 222. For the year 2018, field capacity conditions were assumed to be achieved on DOY 228 since a 107 mm irrigation event took place on DOY 225. Saturation is not necessarily attained after each irrigation or rainfall event. Field capacity is defined as the soil—moisture content reached in an initially thoroughly wet field—that is at or near saturation, after the rate of drainage by gravity has markedly decreased. Field capacity corresponds to the soil moisture content after gravitational water has been drained from the soil. The rate of drainage depends on the soil, but field capacity is typically assumed to occur 24–48 h after thorough wetting by irrigation or rainfall (Taylor and Ashcroft 1972).

The SWSI for the deficit irrigated plot was calculated with MAD of 0.40, based on the recommendation by Panda et al. (2004), suggesting that desirable maize MAD should be less than 45% for maize. MAD was kept the same value of 0.40 for the data being from the end of July to September. Most of the data used on SWSI analysis occurred when maize was near maximum canopy height. Thus, MAD values were assumed not to change drastically, which could allow it to be assumed constant for the entire dataset analyzed. VWC_{WP} was obtained from the United States Natural Resources Conservation Service (NCRS) soil survey website. Soil texture classification followed the range of values provided by Saxton and Rawls (2006) based on values of VWC_{FC} and VWC_{WP} per soil layer of the root zone. Daily SWSI data were initially calculated per soil layer and averaged for each location of measurement. Only days with no occurrence of rainfall or irrigation events were considered to avoid dealing with the three-dimensional redistribution of soil water content

within the root zone for the next days after the soil profile is replenished.

To assess the capabilities of inferring on SWSI based on estimations of CWSI using the energy balance approach, three non-linear empirical models were fitted to the SWSI and CWSI data to identify potential equation types that could be representative on providing information about the level of water stress on the root zone. It was assumed a level of significance of 0.05 for testing the statistical significance of the fitted coefficient estimation. The models for SWSI as a function of estimated CWSI were the following: Weibull, rational, and sum of sine functions as in Eqs. (42), (43), and (44), respectively.

$$SWSI = c_1 c_2 \left[CWSI^{(c_2-1)} \right] \exp \left[-c_1 (CWSI^{c_2}) \right] \qquad (42)$$

$$SWSI = \frac{c_3(CWSI) + c_4}{CWSI^2 + c_5(CWSI) + c_6}, \qquad (43)$$

$$SWSI = c_7 \sin \left[c_8(CWSI) + c_9 \right]. \qquad (44)$$

Independent assessment of the CWSI model

To assess the performance of the proposed CWSI model, independently observed CWSI values were used. These independent observed values were based on sap flow readings; used as a reference to evaluate estimated CWSI (CWSI$_E$). Both CWSI approaches are further detailed below:

(a) Crop water stress index calculated based on Eq. (7) regarding measured R_n, G, and H from surface energy balance (CWSI$_{SEB}$). On-site sensible heat flux measured data were obtained from the Bowen ratio method.

(b) Crop water stress index calculated using Eq. (3), in which ET$_a$ data were obtained from on-site sap flow measurements of canopy transpiration on the deficit irrigated field (area of interest) and ET$_c$ data were collected from sap flow canopy transpiration measurements on the non-stressed field (CWSI$_{sap}$).

Measured surface heat fluxes

Net radiation data were collected using net radiometers at 3.2 m AGL at the stationary locations identified in Fig. 2 in 2017 and 2018.

Measured soil heat flux at the surface level was obtained through the soil heat flux plate method, which consists of measuring the heat flux density at a certain depth in the root zone and accounting for the heat storage on the soil layer above the plate (Ochsner et al. 2006). For each station of measurement, two HFT3-L soil heat flux plates

(Radiation and Energy Balance Inc, Bellevue, WA, USA) were installed, one nearby the maize root zone (west) and another between crop rows (east) at a depth of 8 cm each. Two 5TE soil water content sensors were installed at 4 cm following the same geographical orientation of the soil heat flux plates for determining the stored heat within the soil layer above the plate. Two T107 soil temperature probes (Campbell Scientific, Inc., Logan, UT, USA) were installed at 2 and 6 cm to account for the change in soil temperature over time into the determination of surface soil heat flux.

Measured sensible heat flux through the Bowen ratio method was obtained from the SAT towers installed at the north section of the field in both years. In 2017, the heights of measurement for T_a and RH were 2.60 and 3.20 m AGL. In 2018, the heights of measurement were of 2.60 and 4.20 m AGL. Values of sensible heat flux from the Bowen ratio method were filtered based on the criteria by Perez et al. (1999), which recommend that β_o values must be representative for the measured on-site data time and magnitude. For all surface heat flux measurements, data were collected every minute and averaged over 15 min. Only hourly data around noon (11 am to 3 pm MST), for the measured surface heat fluxes, were considered for the analysis.

Sap flow measurements

Whole plant transpiration was measured with stem heat balance sap flow EXO sensors (Dynamax, Inc, Houston, TX, USA) (Sakuratani 1981). Gages were installed on four representative plants selected at random at different locations within 20 m of each other in both deficit and non-stressed irrigation treatments. Data were collected for approximately 2 months from August through September in both years.

Installation and settings were the same as used by Han et al. (2018). The bottom 2–3 leaves and leaf sheaths were removed a day before installing gages. Sensors were then mounted on stem internodes that were covered with plastic wrap to prevent moisture from stems from entering the sensors. A thin film of silicon was applied to facilitate thermal exchange between the wrapped stem internodes and sensors. Sensors were covered with stretchable and wicking Velcro, and then with waterproof fabric sealed with electrical tape at the top, insulating foam, and finally with insulated foil bubble wrap that was secured with zip ties and sealed with electrical tape at the top. The voltage was set to 4.2 to 4.3 V dc and resulted in power ranging from 0.20 to 0.27 W depending on the size of the sensor. The temperature applied ranged from 0.5 to 4 °C above ambient and there was no stem damage from heat.

The average value of the thermopile radial heat loss factor (K_{sh}) is established when there is low to zero flow and is required to solve the energy balance of the sap flow gages. Average K_{sh} was computed during 3:30–5:30 h MST

(Mountain Standard Time) and set to the daily K_{sh} at 5:30 h. Since the formula for calculating K_{sh} depends on zero sap flow heat flux, there may be a small error in sap flow calculations if there is transpiration during the period used for K_{sh} computation. We estimate that maximum transpiration loss during this period may be 4 g/h based on greenhouse measurements (Comas et al. 2018). If this water loss was entirely from transpiration rather than evaporation, total error from the K_{sh} might be as high as 1.6%, which is not substantial for this application.

Sensor outputs were collected every minute and recorded as 15-min means. Data were screened for abnormalities, which were removed. Sap flow was determined as the mass of water transpired by the plant per unit time (g h^{-1} plant^{-1}) and expressed per ground area by dividing by the planting density. Measurements were averaged per treatment for comparisons with ET estimates from modeled CWSI. Sap flow measurements were considered actual measurements of plant water-use in analyses, and have been previously validated (Dynamax 2016; Comas et al. 2018). Measurements were taken as ET because it was assumed that evaporation from the topsoil was negligible based on the irrigation system type and estimates of CWSI were limited to days without wetting events. The topsoil portion of the root zone was assumed to be the first 20 cm of soil in the root zone profile.

Statistical model analysis

The following statistical variables were calculated to evaluate and compare the results based on statistical approaches to indicate model performance: mean bias error (MBE), root mean square error (RMSE), refined index of agreement (d_r), and Pearson's correlation coefficient (r). MBE and RMSE are indicated by Eqs. (45) and (46), respectively:

$$\text{MBE} = \frac{\sum (E_i - O_i)}{n} \qquad (45)$$

$$\text{RMSE} = \sqrt{\frac{\sum (E_i - O_i)^2}{n}} \qquad (46)$$

where n is the sample size, E_i and O_i mean, respectively, the estimated and measured or observed values. In addition, CWSI MBE and RMSE are presented as percent values. To do this, the NMBE (Normalized Mean Bias Error) measure was chosen. NMBE is a normalization of the MBE index that is used to scale the results of MBE, making them comparable. It quantifies the MBE index by dividing it by the mean of measured values, giving the global difference between the real values and the predicted ones. In the case of RMSE (%), the CV(RMSE) (Coefficient of Variation of the Root Mean Square Error) was adopted. This statistic

measures the variability of the errors between measured and simulated values. It indicates the model's ability to predict the overall load shape that is reflected in the data. The application of NMBE and CV(RMSE) followed the procedure as adopted in Ramos-Ruiz and Fernández-Bandera (2017).

The modified index of agreement, developed by Willmott et al. (2012), is indicated by Eq. (47), where $\bar{E}$ and $\bar{O}$ are the sample mean of estimated and measured or observed values, respectively.

$$d_r = \begin{cases} 1 - \frac{\sum |E_i - O_i|}{2 \sum |O_i - \bar{O}|}, & \sum |E_i - O_i| \leq 2 \sum |O_i - \bar{O}| \\ -1 + \frac{2 \sum |O_i - \bar{O}|}{\sum |E_i - O_i|}, & \sum |E_i - O_i| > 2 \sum |O_i - \bar{O}| \end{cases} . \qquad (47)$$

Pearson correlation coefficient was calculated as following (Ott and Longnecker 2001):

$$r = \frac{\sum (E_i - \bar{E})(O_i - \bar{O})}{\sqrt{\left[\sum (E_i - \bar{E})^2\right]\left[\sum (O_i - \bar{O})^2\right]}} . \qquad (48)$$

Results and discussion

Calibration of soil water content data per root zone layer

The coefficients from each soil water content calibration equation were different between years of measurement because the stations were in different fields in 2017 and 2018 (Tables 2 and 3). The differences in magnitude between stations during the year 2017 indicate that the soil texture and bulk density of the root zone profile change throughout the soil profile.

Soil texture per root zone layer

Soil water content data suggest that soil texture was different between the 0.50 and 0.80 m soil depths in one of the two locations in 2017 and both locations in 2018 (Tables 4 and 5). In 2017, the volumetric water content at field capacity was 38% and 40% greater for station 1.1 than station 1.2, at 0.50 m and 0.80 m depth, respectively.

Substantial differences in field capacity values between the location at a given soil depth might indicate that the soil bulk density is not the same and affects the estimations of measured soil heat flux, soil water deficit, by introducing potential variability on the observed data due to the measurements obtained at a location with different soil characteristic properties.

Table 2 Calibration equation coefficients for soil water content measured with 5TE sensor in 2017

Station ID	Depth (cm)	Response variable	A_1 (slope)	A_2 (interceptor)	N	R^2
1.1	4	TDR	0.403	0.100	7	0.71
	20	NP	1.347	−0.059	11	0.91
	50	NP	0.665	0.071	11	0.89
	80	NP	1.297	−0.067	11	0.92
	110	NP	0.444	0.065	11	0.77
1.2	4	TDR	−0.320	0.155	5	0.94
	20	NP	1.462	−0.068	11	0.87
	50	NP	1.317	−0.022	11	0.96
	80	NP	1.108	−0.013	11	0.93
	110	NP	0.706	0.047	11	0.94

Table 3 Calibration equation coefficients for soil water content measured with 5TE sensor in 2018

Station ID	Depth (cm)	Response variable	A_1 (slope)	A_2 (interceptor)	N	R^2
2.1	4	TDR	1.182	0.028	10	0.91
	20	NP	0.864	0.041	9	0.93
	50	NP	0.673	0.010	16	0.82
	80	NP	1.228	−0.040	13	0.96
	110	NP	1.749	−0.018	9	0.96
2.2	4	TDR	1.424	−0.063	15	0.84
	20	NP	1.462	−0.068	9	0.94
	50	NP	1.000	−0.004	13	0.96
	80	NP	1.799	0.118	14	0.85
	110	NP	1.867	−0.182	9	0.97

Table 4 Summary of root zone characteristics based on VWC data for deficit irrigated field in 2017

		On-site data (NP)	NCRS data		Saxton and Rawls (2006)
Station ID	Depth (cm)	VWC_{FC} (m³/m³)	VWC_{WP} (m³/m³)	VWC_t (m³/m³)	Soil texture
1.1	4	0.167	0.082	0.133	Sandy loam
	20	0.203	0.118	0.169	Sandy loam
	50	0.329	0.113	0.243	Silt loam
	80	0.335	0.167	0.268	Clay loam
	110	0.236	0.054	0.163	Sandy loam
1.2	4	0.230	0.082	0.171	Sandy loam
	20	0.214	0.118	0.176	Sandy loam
	50	0.201	0.113	0.166	Sandy loam
	80	0.202	0.054	0.143	Sandy loam
	110	0.202	0.054	0.143	Sandy loam

Crop root zone tends to expand into deeper soil depths to obtain water when sandy soil texture type is predominant (Jackson et al. 2000). Overall, there would be a potential for significant large values for CWSI based on lighter soil type, since the depletion of water is higher than that for heavy soil texture (Saxton et al. 1986) and the release of water to plants might affect the biophysical processes that regulate transpiration.

Table 5 Summary of root zone characteristics based on VWC data for deficit irrigated field in 2018

| Station ID | Depth (cm) | On-site data (NP) | NCRS data | | Saxton and Rawls (2006) |
		VWC_{FC} (m^3/m^3)	VWC_{WP} (m^3/m^3)	VWC_t (m^3/m^3)	Soil texture
2.1	4	0.195	0.082	0.150	Sandy loam
	20	0.229	0.118	0.185	Sandy loam
	50	0.145	0.082	0.120	Loamy sand
	80	0.163	0.054	0.120	Sandy loam
	110	0.266	0.145	0.218	Clay loam
2.2	4	0.223	0.082	0.167	Sandy loam
	20	0.197	0.118	0.165	Sandy loam
	50	0.136	0.082	0.114	Loamy sand
	80	0.302	0.174	0.251	Clay loam
	110	0.266	0.145	0.218	Clay loam

Soil water stress index assessment

The year of 2018 was drier than 2017, based on the number and magnitude of rainfall events indicated in Fig. 4. Drier seasons allow the crop to undergo water stress conditions for more extended periods than when multiple wetting events occur. Thus, the SWSI in 2018 indicates trends of increased SWSI for longer periods than SWSI in 2017. Different soil types affect the capacity of water to be available for extraction by the plants. The different soil types in which the data were collected could explain the differences in SWSI between two locations within the same field in 2017.

Regarding 2017 data, the location of stations 1.1 and 1.2 provided VWC data from different soil textures at deeper soil layers, as indicated by Table 4. The presence of heavy soil textures at 50 and 80 cm depths at location 1.1 suggests that the overall soil specific area is higher than that at station 1.2. At any given matric potential, clayey soils tend to have higher volumetric soil water content compared to sandy soils. Thus, SWSI at station 1.1 may be lower than at station 1.2, a location characterized by a more homogeneous sandy soil type. For 2018, the soil texture between stations 2.1 and 2.2 was very similar and allowed the SWSI vs. DOY scattered points to follow a trend, which is indicated
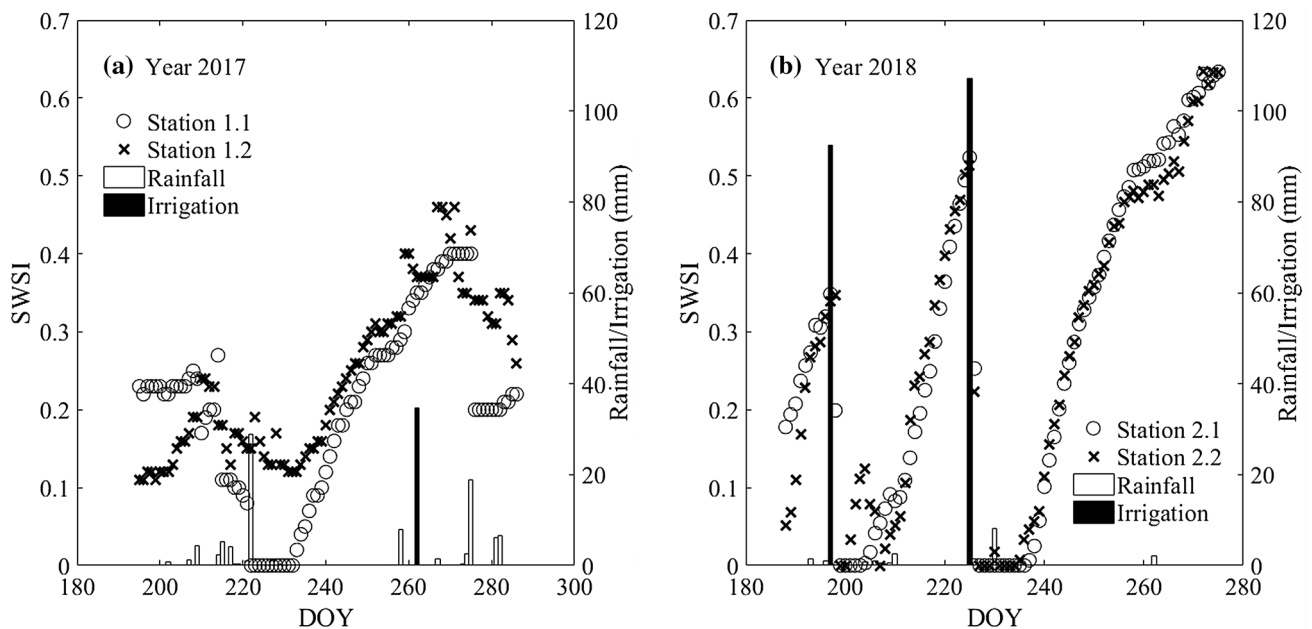

Fig. 4 Comparison between SWSI from the point-measurement locations in 2017 and 2018 at LIRF. **a** Indicates the SWSI vs. DOY for 2017 data. **b** Shows the SWSI vs. DOY for 2018 data
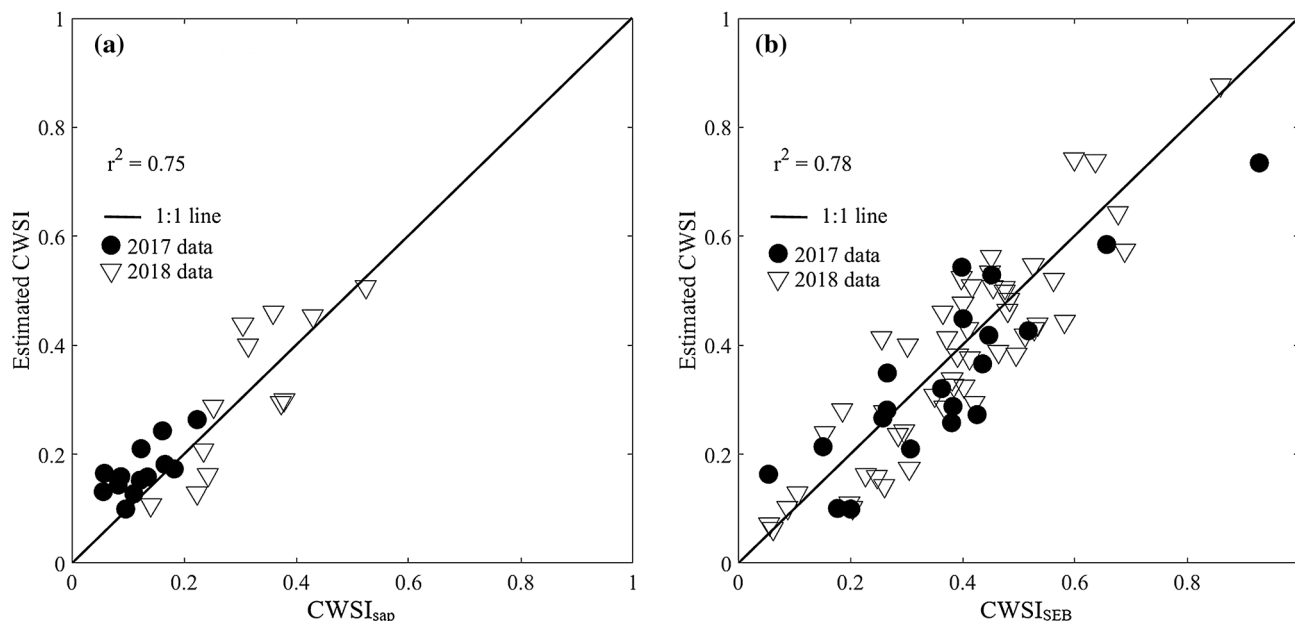
Fig. 5 Observed CWSI vs. estimated CWSI for 2017–2018 data. **a** Represents the plot regarding observed CWSI determined through transpiration measurements. **b** Shows the plot regarding observed CWSI determined through measured surface heat fluxes (R_n, G, H)

in Fig. 4b. After major irrigation events, the SWSI on both locations decreased significantly reaching values near zero, which suggests no stress conditions on the days following the wetting event. Rainfall events seemed to have less effect on the SWSI in 2018 than 2017 since there is no evidence of changes in stress conditions after rainfall replenished the soil profile. The magnitude of rainfall water depth, compared to the irrigation water depth application, was overall only 9% of the most significant irrigation event on DOY 225 in 2018. In 2017, the average ratio between rainfall and irrigation amounts was 54%, which indicates an active contribution of both rainfall and irrigation amounts toward attenuating the water stress conditions in 2017 at stations 1.1 and 1.2.

Crop water stress index model assessment

The estimated CWSI based on modeled or estimated surface heat fluxes ($CWSI_E$), when evaluated with $CWSI_{sap}$, provided an MBE of 0.02 and an RMSE of 0.06, with corresponding NMBE of 8.7% and CV RMSE of 29.1% (Table 6).

Overall is a small mean error with a somewhat larger error spread. However, most of the spread in the errors (around mean values) come from one overestimated CWSI value on 09/03/17 of 133.9%. This value was not flagged as an outlier because it is within three standard deviations of mean values. Furthermore, some discrepancy between CWSI obtained with the proposed (H) method and that of the sap flow measurements is expected due to sampling area differences (larger area integrated by temperature measurements vs. individual plants, respectively). When the analysis was done comparing $CWSI_E$ with $CWSI_{SEB}$, MBE was − 0.02, and RMSE was 0.09, with corresponding NMBE of − 4.2% and CV RMSE of 19.5% (Table 6). The footprint (heat flux area contribution) for the Bowen ratio method was somewhat larger than that for the proposed "H" method due to the location of the measuring stations/sensor. However, this comparison is more appropriate (than that for the Sap flow derived CWSI) because both methods are sampling (integrating) areas (instead of point measurements). The resulting error, for this comparison, is considered acceptable. The

Table 6 Summary of CWSI model performance regarding independent CWSI data for deficit irrigated field at LIRF in 2017–2018

Independent CWSI	MBE	NMBE (%)	RMSE	CV RMSE (%)	Sample size (n)	D_r	Pearson's r
Equation (3) using canopy transpiration data (sapflow)	0.02	8.7	0.06	29.1	25	0.75	0.87
Equation (7) using measured surface heat fluxes	− 0.02	− 4.2	0.09	19.5	71	0.71	0.88

refined index of agreement for both CWSI model performances was higher than 0.70, which indicates satisfactory agreement between estimated and observed CWSI values based on the samples analyzed. Pearson's correlation coefficient r was 0.87 and 0.88 for the comparison of $CWSI_E$ to $CWSI_{sap}$ and $CWSI_{SEB}$, respectively. Evans (1996) suggests that Pearson's r values greater than 0.80 must indicate a strong correlation between variables.

The proposed model for CWSI seems to provide a statistical analysis that results in small RMSE for both independently observed CWSI datasets. Overestimation or underestimation of conditions may occur depending on the nature of the derivation of observed CWSI. For the case when estimated CWSI is compared to observed CWSI based on canopy transpiration data, overestimation seems to occur. Underestimation of CWSI is evident when estimated values of CWSI are compared to observed CWSI data from measured R_n, G, and Bowen ratio H. The underestimation and overestimation of estimated values for CWSI might be explained based on limitations on the models for R_n, G, and H to capture all magnitude of their respective measured values (Fig. 5).

On average, the estimated values for CWSI were 4% smaller than observed CWSI based on measured R_n, G, and Bowen ratio H. If 2017 and 2018 data are analyzed separately, modeled CWSI was 8% and 2% smaller than CWSI from measured heat fluxes, respectively. When estimated CWSI is compared to observed CWSI based on biomass transpiration (sap flow), modeled values for CWSI were 10% greater than observed values, on average.

Estimated $CWSI_E$ and SWSI relationship

The SWSI model based on Eq. (42) presents a strong statistical evidence that the fitted coefficients c_1 and c_2 are representative of characterizing the non-linear relationship between daily SWSI and estimated CWSI because the respective p values are less than 0.05 (Table 7). The

modeling for SWSI based on Eqs. (43) and (44) did not have all fitted coefficient estimation with significant statistical evidence. For the SWSI model based on the rational function approach, all p values were greater than 0.05. Regarding the SWSI model based on Eq. (44), only the fitted coefficient c_9 did not provide a good statistical evidence. The degrees of freedom might be a factor that is not allowing SWSI models based on Eqs. (43) and (44) to have all proper coefficient estimations with enough evidence to validate the relationship between SWSI and estimated CWSI.

From Fig. 6, the curve fitting models gradually follow up the trend of data points. SWSI and CWSI are related to the concept of water stress, which is based on the depletion of water from the root zone. As the water in the soil reaches levels below the defined VWC_t over time for a given MAD, the magnitude of SWSI and CWSI tends to increase, with the exception when a recharge event (e.g., rainfall or irrigation) occurs. All SWSI models plotted in Fig. 6 seem to fit the data well up to a specific range of CWSI. However, the curve fitting upper and lower tails have different characteristics. For the Fig. 6a and c, regarding the SWSI model used, Eqs. (42) and (44), respectively, there is an offset of the curve on the lower tail when CWSI is/tends to zero. This result means that the models based on the Weibull and sum of sine indicate that there might be SWSI conditions even when crop water stress could be assumed negligible or zero. This result can occur when advection occurs with strong winds. Equation (43) for estimating SWSI based on the rational function seems to adjust better to the condition when CWSI and SWSI are zero (no or minimal soil water stress).

The upper tail also has differences among all SWSI models analyzed. Weibull function model indicated by Fig. 6a seems to keep the trend of increasing estimation of SWSI as CWSI continues to increase. The SWSI curve fitting based on Eqs. (43) and (44) does not have the same behavior. Figure 6b seems to reach a constant level of soil water stress for when CWSI values are equal or greater than 0.70, which

Table 7 Non-linear regression statistics regarding models for SWSI based on estimated CWSI

| SWSI model	Number of observations	Degrees of freedom	Fitted coefficient	Estimate	Standard error	Test-statistic	P value
Weibull function (Eq. 42)	39	37	c_1	0.46307	0.01443	32.095	1.2943e−28
			c_2	1.80940	0.05341	33.878	1.8686e−29
Rational function (Eq. 43)	39	35	c_3	0.77008	0.57028	1.350	0.1856
			c_4	−0.00849	0.03445	−0.246	0.8068
			c_5	−0.02234	0.84006	−0.027	0.9789
			c_6	0.63463	0.23324	2.721	0.0101
Sum of sine (Eq. 44)	39	36	c_7	−0.49153	0.01622	−30.307	3.2078e−27
			c_8	−2.15270	0.16602	−12.966	3.9441e−15
			c_9	−0.01345	0.04220	−0.319	0.7518
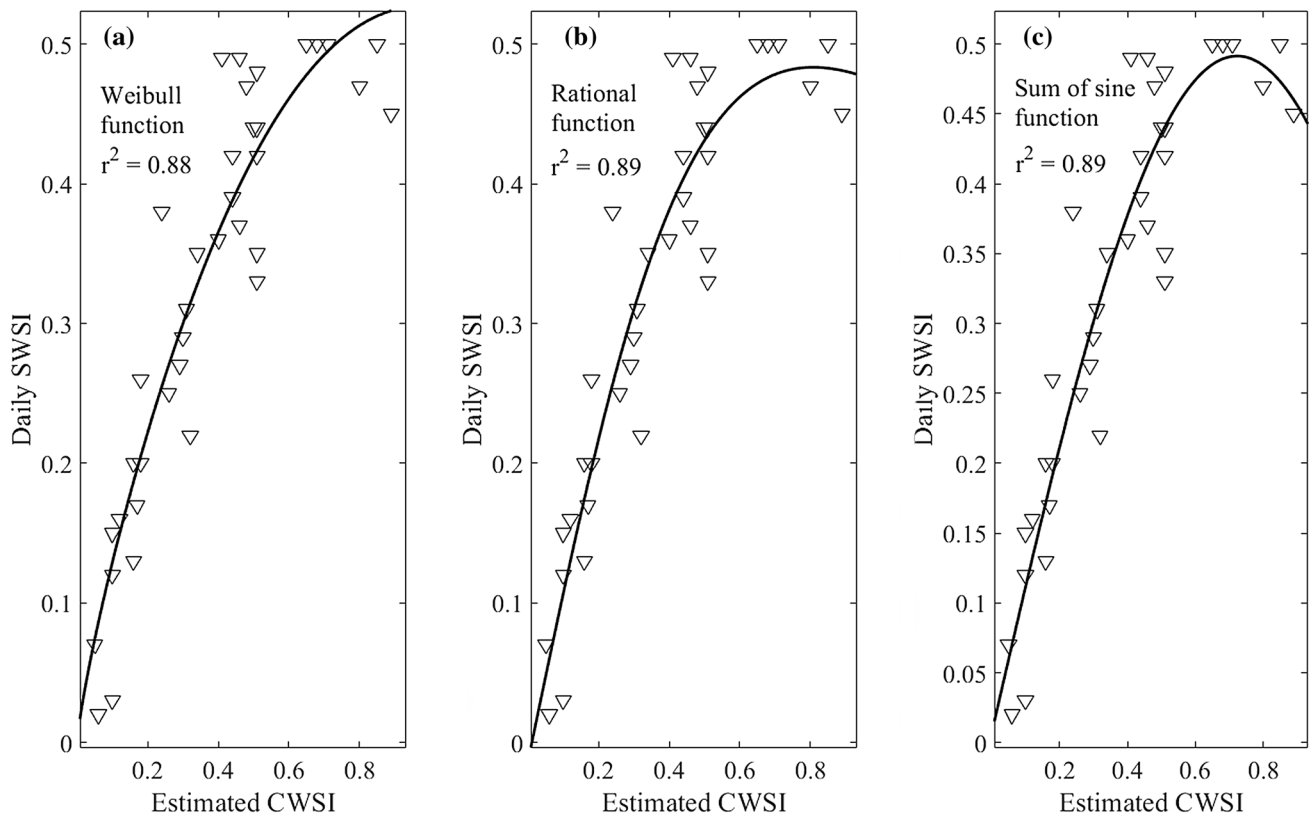
Fig. 6 Estimated CWSI vs. Daily SWSI at deficit irrigated plots at LIRF regarding 2017–2018 data. **a–c** Show, respectively, the empirical models based on Eqs. (42), (43), and (44)

agrees with the concept of water depletion based on SWSI developed by Chávez (2015). It might be assumed that for levels of soil water depletion that surpasses the critical VWC for the imminence of stress, the values of VWC_a will not change significantly over time if wetting events do not occur. Therefore, SWSI values tend to remain constant later in the season. For SWSI based on the sum of the sine approach, Fig. 6c shows that when CWSI is greater than 0.70, the respective curve starts to decline. High values of CWSI might occur by the end of the growing season when the plants are not biologically active, and transpiration and evaporation are very limited due to plant physiology and water availability in the root zone, under dry weather conditions.

Fitted curves (models) present two different CWSI values for the same SWSI levels for values between of CWSI between 0.5 and 0.9 (e.g., for fitting model based on the sum of sine function, Fig. 6c). It is not feasible that for a larger CWSI level, there would be less SWSI. Thus, it is appropriate to conclude that there is a larger uncertainty on CWSI and SWSI values estimated and calculated for large soil water deficits and crop water stress levels and that the models, especially the SWSI model based on Eq. (42) (Fig. 6b), should be limited to CWSI values of to 0.7. It seems the

model based on the rational function characterizes the physical system better than the other two models analyzed.

Conclusions

The study indicates that there exists statistical evidence showing that the proposed estimation of CWSI based on the relationship between sensible heat flux and available energy performs well. The approach seems to be an alternative method, and it may facilitate the incorporation of remote sensing approaches to scale CWSI to large fields and irrigation districts to improve irrigation scheduling and conserve water resources. The CWSI models applied resulted in relatively small MBE and RMSE values and high correlation coefficients between observed and estimated values. This result indicates that the sensible heat flux modeling approaches based on the surface aerodynamic temperature could be useful for predicting the stress level of row crops based on the relationship between H and $(R_n - G)$. It seems that the approach developed for estimating sensible heat flux, based on aerodynamic surface temperature, has the capability to indicate the stress conditions of the canopy. The small average available energy and Bowen ratio-derived sensible

heat flux uncertainties of $(400.7 \text{ W/m}^2) \pm 8.5 \text{ W/m}^2$ and $(160.7 \text{ W/m}^2) \pm 6.6 \text{ W/m}^2$, respectively, suggest the potential applicability of the evaluated CWSI model.

Differences in soil texture across a given field are sources of variability when determining SWSI and CWSI based on the energy balance approach due to the water holding capacity and soil-specific area differences. When treating the area of interest as a lumped system (point in space), the variations in texture are neglected and bias is introduced on the assessment of the models due to the input variables being not able to accommodate the heterogeneity of the soil. Assessing SWSI based on estimated CWSI from the energy balance approach investigated in this paper seems to be applicable. The models based on Weibull, rational, and sum of sine functions seem to behave similarly for a specific range of CWSI. The non-linear relationship, between SWSI and CWSI, is better characterized by the empirical model indicated by Eq. (43); which is based on a rational polynomial function. There is strong statistical evidence that SWSI and CWSI are statistically related through a non-linear approach and that estimates of CWSI might be valuable information to assess soil water stress levels throughout the crop root zone.

Compliance with ethical standards

References

Allen RG, Pereira LS, Raes D, Smith M (1998) Crop evapotranspiration—guidelines for computing crop water requirements. FAO Irrigation and drainage paper 56. Food and Agriculture Organization, Rome

ASCE-EWRI (2005) The ASCE Standardized Reference Evapotranspiration Equation. Report 0-7844-0805-X, ASCE Task Committee on Standardization of Reference Evapotranspiration. Reston, Va., American Soc. Civil Engineers

Bastiaanssen WGM, Menenti M, Feddes RA, Holtslag AAM (1998) A remote sensing surface energy balance algorithm for land (SEBAL): 1. Formulation. J Hydrol 212–213:198–212

Ben-Gal A, Agam N, Alchanatis V, Cohen Y, Yermiyahu U, Zipori I, Presnov E, Sprintsin M, Dag A (2009) Evaluating water stress in irrigated olives: correlation of soil water status, tree water status, and thermal imagery. Irrig Sci 27:367–376

Bowen IS (1926) The ratio of heat losses by conduction and by evaporation from any water surface. Phys Rev 27:779–787

Brunsell NA, Gillies R (2002) Incorporating surface emissivity into a thermal atmospheric correction. Photogramm Eng Remote Sens J 68:1263–1269

Brutsaert W (1975) On a derivable formula for long-wave radiation from clear skies. Water Resour Res 11(5):742–744. https://doi.org/10.1029/WR011i005p00742

Brutsaert W (1982) Evaporation into the atmosphere. D. Reidel Publication

Chávez JL (2015) Using canopy temperature as an indicator of plant stress. In: Proceedings of the 27th Annual Central Plains Irrigation Conference (CPIC), Colby, KS, February 17–18, 2015, CPIA, 760 N. Thompson, Colby, Kansas, February 17–18

Chávez JL, Howell TA, Gowda PH, Copeland KS, Prueger JH (2010) Surface aerodynamic temperature modeling over rainfed cotton. Trans ASABE 53(3):759–767

Choudhury BJ, Monteith JL (1988) A four-layer model for the heat budget of homogeneous land surfaces. Q J R Meteorol Soc 114(480):373–398

Chung U, Gbegbelegbe S, Shiferaw B, Robertson R, Yun JI, Tesfaye K, Hoogenboom G, Sonder K (2014) Modeling the effect of a heat wave on maize production in the USA and its implications on food security in the developing world. Weather Clim Extremes J 5–6:67–77

Comas LH, van Bavel MG, Young JS, Chesus KA (2018) Improved installation and validation of sap flow sensors on maize plants. Acta Hort 1222:167–172

Costa-Filho E (2019) Modeling sensible heat flux for vegetated surfaces through an optimized surface aerodynamic temperature approach. M.Sc. Thesis. Colorado State University, Fort Collins, CO, USA, 156 pp

Crawford TM, Duchon CE (1999) An improved parameterization for estimating effective atmospheric emissivity for use in calculating daytime downwelling longwave radiation. J Appl Meteor 38:474–480

Dynamax (2016) Installation of sap flow sensor on maize plants. http://www.dynamax.com/images/uploads/papers/Corn-Installation-SGEX.pdf. Accessed 12 September 2019

Ehrler WL, Idso SB, Jackson RD, Reginato RJ (1978) Diurnal changes in plant water potential and canopy temperature of wheat as affected by drought. Agron J 70:999–1004

Evans JD (1996) Straightforward statistics for the behavioral sciences. Brooks/Cole Publishing, Pacific Grove

Garcia LA, Elhaddad A, Altenhofen J, Hattendorf M (2013) Developing corn regional crop coefficients using a satellite-based energy balance model (ReSET-RASTER) in the south platte river basin of Colorado. J Irrig Drain Eng 139:821–832

Gardner RW, Ehlig CF (1963) The influence of soil water on transpiration by plants. J Geophys Res 68:5719–5724

Han M, Zhang H, DeJonge KC, Comas LH, Gleason S (2018) Comparison of three crop water stress index models with sap flow measurements in maize. Agric Water Manag 203:366–375

Idso SB, Jackson RD, Reginato RJ (1977) Remote sensing of crop yields. Science 196:19–25

Idso SB, Jackson RD, Pinter PJ, Reginato RJ, Hatfield JL (1981) Normalizing the stress–degree–day parameter for environmental variability. Agric Meteorol J 24:45–55

Jackson RD, Idso SB, Reginato RJE, Pinter PJ (1981) Canopy temperature as a crop water stress indicator. Water Resour Res 17:1133–1138

Jackson RD, Kustas WP, Choudhury BJ (1988) A reexamination of the crop water stress index. Irrig Sci 9:309–317. https://doi.org/10.1007/BF00296705

Jackson RB, Sperry JS, Dawson TE (2000) Root water uptake and transport: using physiological processes in global predictions. Trends Plant Sci 5(11):482–488

Jiang Y, Jiang X, Tang R, Li ZL, Zhang Y, Huang C, Ru C (2018) Estimation of daily evapotranspiration using instantaneous decoupling coefficient from the MODIS and field data. IEEE J Selected Topics Appl Earth Observ Remote Sens 11(6):1832–1838

Johnson LF, Trout TJ (2012) Satellite NDVI assisted monitoring of vegetable crop evapotranspiration in California's San Joaquin valley. Remote Sens 4(2):439–455

Jones HG (1999) Use of infrared thermometry for estimation of stomatal conductance as a possible aid to irrigation scheduling. Agric For Meteorol 95(3):139–149

Monin AS, Obukhov AM (1954) Basic laws of turbulent mixing in the atmosphere near the ground. Trudy Geofiz Inst AN SSSR 24(151):163–187

Ochsner TE, Sauer TJ, Horton B (2006) Field tests of the soil heat flux plate method and some alternatives. Agron J 98:1005–1014

O'Shaughnessy SA, Evett SR, Colaizzi PD, Howell TA (2011) Using radiation thermography and thermometry to evaluate crop water stress in soybean and cotton. Agric Water Manag 98:1523–1535

Osroosh Y, Peters RT, Campbell CS, Zhang Q (2015) Automatic irrigation scheduling of apple trees using theoretical crop water stress index with an innovative dynamic threshold. Comput Electron Agric 118:193–203

Ott RL, Longnecker M (2001) An introduction to statistical methods and data analysis. Cengage Learn, Boston

Panda RK, Behera SK, Kashyap PS (2004) Effective management of irrigation water for maize under stressed conditions. Agric Water Manag 66(3):181–203

Perez PJ, Castellvi F, Ibanez M, Rosell JI (1999) Assessment of reliability of Bowen ratio method for partitioning fluxes. Agric For Meteorol 97(3):141–150

Ramos-Ruiz G, Fernández-Bandera C (2017) Validation of calibrated energy models: common errors. Energies 10:1587. https://doi.org/10.3390/en10101587

Rondeaux G, Steven M, Baret F (1996) Optimization of soil-adjusted vegetation indices. Remote Sens Environ 55:95–107

Sagayo S, Ovando G, Bocco M (2017) Landsat images and crop model for evaluating water stress of rainfed soybean. Remote Sens Environ 198:30–39

Sakuratani T (1981) A heat balance method for measuring water flux in the stem of intact plants. J Agric Meteorol 31:9–17

Saxton KE, Rawls WJ (2006) Soil water characteristic estimates by texture and organic matter for hydrologic solutions. Soil Sci Soc Am J 70:1569–1578

Saxton KE, Rawls WJ, Romberger JS, Papendick RI (1986) Estimating generalized soil–water characteristics from texture. Soil Sci Soc Am J 50(4):1031–1036

Taiz L, Zeiger E, Moller IM, Murphy A (2015) Plant physiology and development. Sinauer Associates Inc, Sunderland

Taylor SA, Ashcroft GL (1972) Physical edaphology. W. H. Freeman and Co, San Francisco

Tubiello FN, Rosenzweig C, Goldberg RA, Jagtap S, Jones JW (2002) Effects of climate change on US crop production: simulation results using two different GCM scenarios. Part I: wheat, potato, maize, and citrus. Clim Res 20:259–270

USDA, NASS (2017) Corn and soybeans production up in 2016, USDA reports. http://nass.usda.gov/Newsroom/printable/2017/01_12_17.pdf. Accessed 10 Dec 2019

Wang R, Bowling LC, Cherkauer KA (2015) Estimation of the effects of climate variability on crop yield in the Midwest USA. Agric For Meteorol 216:141–156

Wang R, Cherkauer K, Bowling L (2016) Corn response to climate stress detected with satellite-based NDVI time series. Remote Sens 8(4):269

Willmott CJ, Robeson SM, Matsuura K (2012) A refined index of model performance. Int J Climatol 32:2088–2094

Yasuda N (1988) Turbulent diffusivity and diurnal variations in the atmospheric boundary layer. Bound-Layer Meteorol 43:209–221

Zarco-Tejada PJ, Gonzalez-Lugo V, Williams LE, Suarez L, Berni JAJ, Goldhamer D, Fereres E (2013) A PRI-based water stress index combining structural and chlorophyll effects: assessment using diurnal narrow-band airborne imagery and the CWSI thermal index. Remote Sens Environ 138:38–50